MATERIALS SCIENCE

Ultrafast correlated charge and lattice motion in a hybrid metal halide perovskite

Yang Lan[1], Benjamin J. Dringoli[1], David A. Valverde-Chávez[1], Carlito S. Ponseca Jr.[2], Mark Sutton[1], Yihui He[3], Mercouri G. Kanatzidis[3], David G. Cooke[1]*

Hybrid organic-inorganic halide perovskites have shown remarkable optoelectronic properties, exhibiting an impressive tolerance to defects believed to originate from correlated motion of charge carriers and the polar lattice forming large polarons. Few experimental techniques are capable of directly probing these correlations, requiring simultaneous sub–millielectron volt energy and femtosecond temporal resolution after absorption of a photon. Here, we use time-resolved multi-THz spectroscopy, sensitive to the internal excitations of the polaron, to temporally and energetically resolve the coherent coupling of charges to longitudinal optical phonons in single-crystal $CH_3NH_3PbI_3$ (MAPI). We observe room temperature intraband quantum beats arising from the coherent displacement of charge from the coupled phonon cloud. Our measurements provide strong evidence for the existence of polarons in MAPI at room temperature, suggesting that electron/hole-phonon coupling is a defining aspect of the hybrid metal-halide perovskites contributing to the protection from scattering and enhanced carrier lifetimes that define their usefulness in devices.

INTRODUCTION

Electron-phonon coupling appears to play a substantial role in defining the optoelectronic properties of hybrid organic-inorganic halide perovskites (*1*–*6*). The perovskite lattice, with chemical formula ABX_3, is composed of an octahedrally coordinated metal-halide BX_3 sublattice and an organic A-site cation that displays dynamic disorder due to "soft" noncovalent bonding. This results in a complex vibrational landscape in a highly polar material. A charge moving in such a polar lattice causes a local distortion as atoms move in response to the Coulomb perturbation (*7*–*9*). This charge and coupled lattice distortion move as a single quasiparticle called a polaron (*1*, *10*–*15*). Dynamic screening of electron-hole Coulomb interactions by the motion of the polar lattice can lower scattering and recombination rates (*16*), which may explain the significant carrier mobilities in defect-heavy solution–processed films and long carrier lifetimes beyond that of a simple direct bandgap semiconductor. Ultrafast Kerr, Raman, and two-dimensional (2D) electronic spectroscopy measurements have shown coherent nuclear vibrational dynamics impulsively coupled to electronic interband transitions (*9*, *12*, *14*, *17*–*21*). Electronic coherence, however, is typically not observed, dominated instead by a solvation-like response suggesting dynamic screening by the freely rotating organic cation (*12*) or by the anharmonic response of the perovskite structure itself (*17*). Terahertz (THz) spectroscopy, which probes intraband carrier motion, has shown a delayed onset of photoconductivity, taking several hundreds of femtoseconds to reach a maximum. This was initially interpreted as a signature of exciton dissociation (*22*, *23*); however, more recently, it has been assigned to the dressing of charge carriers by longitudinal optical (LO) phonons, forming a large polaron that reduces momentum scattering while also increasing the carrier effective mass (*24*). THz emission from perovskite films also shows coherent vibrational dynamics at a lower LO phonon energy of 1.2 THz (*25*). There is uncertainty in the nature of polaron formation in these perovskite materials, as well as the role that each phonon plays in its stabilization (*26*).

[1]Department of Physics, McGill University, Montreal, QC H3A 2T8, Canada. [2]Division of Biomolecular and Organic Electronics, IFM, Linköpings Universitet, Linköping SE- 58183, Sweden. [3]Department of Chemistry, Northwestern University, Evanston, IL 60208, USA.
*Corresponding author. Email: cooke@physics.mcgill.ca

In this work, we use time-resolved multi-THz spectroscopy (TRTS) to probe the correlated motion of charges in single-crystal $CH_3NH_3PbI_3$ (MAPI) at room temperature. A schematic of the experiment is shown in Fig. 1A, where an optical pump pulse resonant with the band edge injects charge carriers, and the intraband polarization is probed by reflection of a single-cycle, ultrabroadband THz pulse at delay time τ after photoexcitation. Phase-resolved detection of the THz pulse electric field allows the resolution of each Fourier component within the pulse (amplitude and phase) with sub–millielectron volt energy resolution and the dynamics of their modulation tracked with a 35-fs temporal resolution (*27*). We use this capability to resolve the coherent motion of charge carriers correlated with the motion of the polar lattice of MAPI, as polarons are formed on a time scale commensurate with the LO phonon period after band-edge excitation.

RESULTS AND DISCUSSION

A coherence in the electronic motion is launched by impulsive excitation at the band edge by the pump pulse, and the THz pulse probes the evolution of the coherent intraband polarization along the pump-probe delay axis. There are two contributions to the intraband polarization: the center-of-mass motion of the charge and the internal excitation spectrum of the polaron (*28*). The THz pulse probes the polaron spectrum via a three-body scattering process whereby a THz photon is absorbed, leaving it excited and emitting an LO phonon. While the center-of-mass motion of the charge can respond to any harmonic mode of the THz probe, the internal charge motion of the polaron has a characteristic excitation energy of $\hbar\omega_{LO}$. For THz frequencies $\omega < \omega_{LO}$, only the center-of-mass motion of the charge particle is probed, and no interference between these motions is observed (see Fig. 1C). However, for $\omega > \omega_{LO}$ (Fig. 1D), the internal motion of charge relative to the LO phonon cloud also contributes causing the intraband polarization, and subsequently the THz reflectivity amplitude, to display a coherent beat along the pump-probe time axis at a frequency $\omega_{osc} = |\omega - \omega_{LO}|$. Near resonance, $\omega \approx \omega_{LO}$, a small oscillation is expected for a frequency range defined by the uncertainty relation and the lifetime of the LO phonon. A π phase flip in the relative displacement is expected when ω crosses resonance. The 35-fs optical excitation impulsively launches

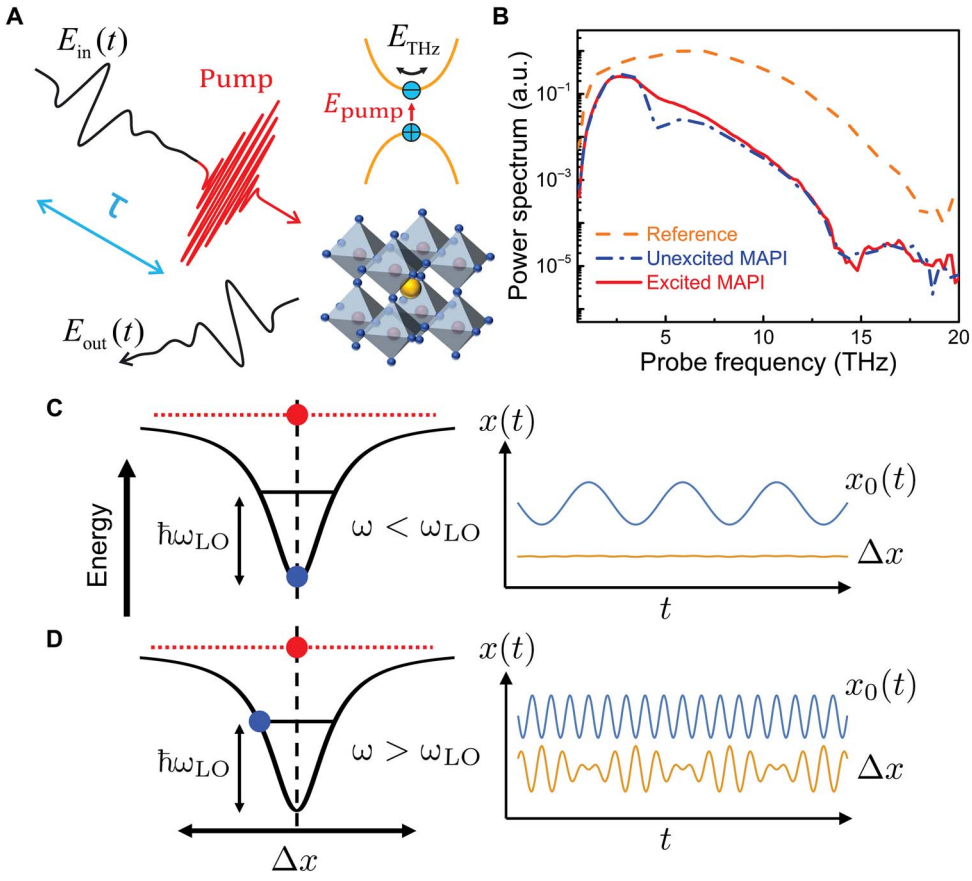

Fig. 1. TRTS measurement and intraband polarization response of the polaron. (**A**) Schematic of TRTS on single-crystal MAPI in reflection configuration with pump-probe delay time τ. (**B**) Reflected THz power spectrum from a metallic mirror (orange dashed curve), unexcited MAPI (blue dashed and dotted curve), and MAPI photoexcited at τ = 1 ps (red solid curve). Schematic of the internal motion of a driven charge (blue dot) at frequency ω coupled to an LO polar lattice distortion with phonon frequency ω_{LO} for frequencies below (**C**) and above (**D**) resonance, with the accompanying motion of the bare charge (red dot), $x_0(t)$, and the relative displacement $\Delta x(t)$ showing a beat. a.u., arbitrary units.

phase-coherent motion for probe energies below ~10 THz, and scanning the pump-probe delay τ maps the time evolution of this coherent beat until it dephases because of interactions. Following injection of charge, coherent LO phonons are in general emitted upon the formation of a polaron, and these can participate in all scattering processes including those that lead to THz interactions with polaron-excited states. The influence of coupled plasmon–LO phonon modes is likely negligible as the bulk plasma frequency $\omega_p/2\pi$ is approximately 50 THz, well outside of our spectral window.

The reflected THz pulse power spectrum from the crystal at negative pump-probe delays, before the pump pulse has arrived, is shown in Fig. 1B along with the τ = 1 ps spectrum. As in previous work (*23*), the unpumped power spectrum is dominated by a dip at ω ~ (2π) 4.8 THz because of a reflectivity minimum on the high-frequency edge of the reststrahlen band, which occurs between the transverse optical (TO) phonon at ω_{TO} = (2π) 2 THz and the LO phonon at ω_{LO} = (2π) 3.7 THz (*23*, *29*, *30*). Upon excitation, mobile charge carriers move to screen the polar lattice, eliminating the 4.8-THz dip in the reflected THz pulse, as shown in the red line in Fig. 1B. The amplitude of the differential THz reflectivity, $|\Delta r(\omega, \tau)|/|r_0|$, is therefore strongly peaked at the nearby frequency of 4.6 THz, as shown in the fixed τ slices of the 2D map in Fig. 2A. We have verified that the THz field used in these measurements, whose peak field is below 20 kV/cm, is within the linear response regime (see the Supplementary Materials).

Close inspection of the early time dynamics in the $|\Delta r(\omega, \tau)|/|r_0|$ map in Fig. 2B shows coherent oscillations appearing along the pump-probe delay axis for frequencies higher than the main reflectivity peak, superimposed on an approximately exponential, subpicosecond rise to the steady state. These oscillations reflect the internal motion of the charge within the polaron. 1D delay time cuts for fixed ω are shown in Fig. 2 (C to F) for probe energies indicated in Fig. 2B. At the lowest frequency of ω = (2π) 1.2 THz in Fig. 2C, just above the Pb-I–related TO phonon at 1 THz (*29*, *30*) and in a region where the contribution of the polar lattice dominates, the differential reflectivity is small, as the injected charge is a weak perturbation relative to the reflectivity of the unexcited lattice. No oscillations are observed in this case within the limit of scan time. At ω = (2π) 2.9 THz (12 meV) in Fig. 2D, the sign of the steady-state differential reflectivity is initially positive but rapidly turns negative within 250 fs. A negative $|\Delta r|/|r_0|$ is expected in this region, as mobile carriers move to screen lattice motion, reducing the reflectivity relative to the unexcited state. In Fig. 2E, ω = (2π) 4.6 THz, where the lattice is least polarizable, small oscillations are superimposed on the monotonically increasing signal. At ω = (2π) 7.5 THz in Fig. 2F, electronic contributions dominate and high-frequency oscillations are observed lasting for several periods. This response was seen for all crystal facets examined (data provided in the Supplementary Materials).

The slow contributions to the signal can be well described by an exponential rise convoluted with a Gaussian instrument response

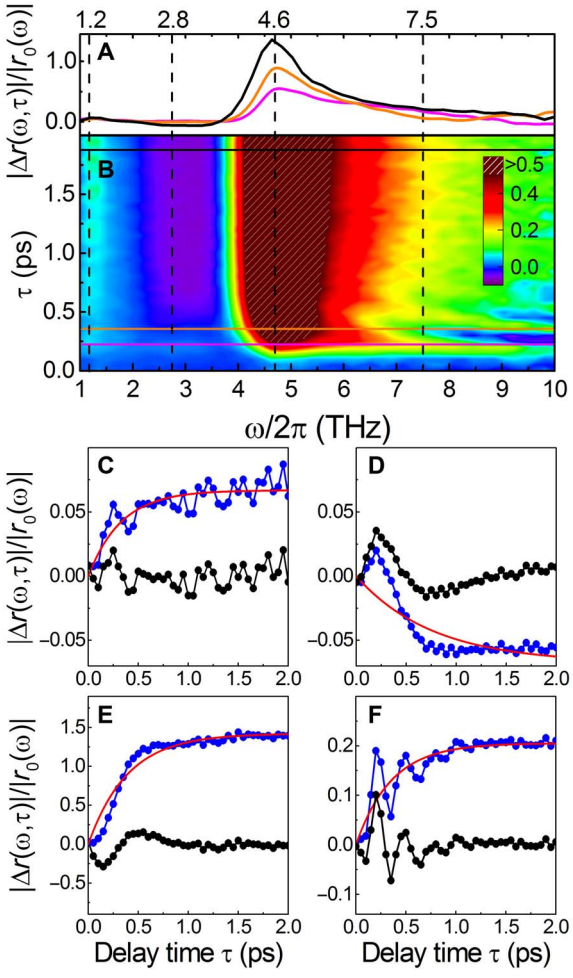

Fig. 2. Time-resolved THz reflectivity from MAPI after band-edge optical excitation. (**A**) Differential reflectivity $|\Delta r(\omega,\tau)|/|r_0|$ cuts at selected delay times τ marked in (B). (**B**) 2D-probe frequency/delay time color scale map for $|\Delta r(\omega,\tau)|/|r_0|$. (**C** to **F**) $|\Delta r(\omega,\tau)|/|r_0|$ at the four probe frequencies 1.2, 2.8, 4.6, and 7.5 THz, respectively. The differential reflectivity amplitude is represented by blue curves, the fitted background exponential change is shown in red, and the differential reflectivity oscillations obtained by subtracting the slow exponential rise are shown in black.

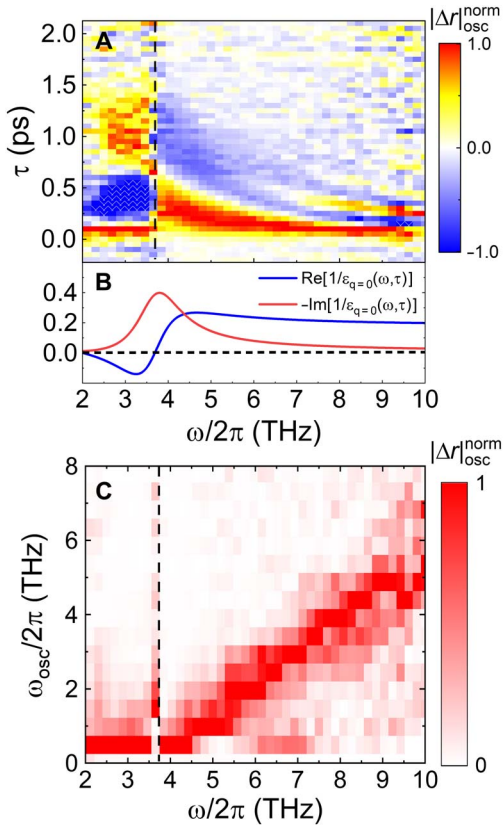

Fig. 3. Coherent oscillations of THz reflectivity without slow rise component. (**A**) Normalized $|\Delta r(\omega,\tau)|^{norm}_{osc}$ map with slow rise component subtracted. The vertical dashed line marks the LO phonon frequency at 3.7 THz, where a π phase flip occurs and above which a subsequent frequency chirp is evident. (**B**) Schematic dielectric energy loss function describing inelastic optical phonon scattering and screening function describing the renormalization of dressed charges for MAPI. (**C**) Fourier transformation along delay time axis τ, $|\Delta r(\omega,\omega_{osc})|^{norm}_{osc}$, showing an onset of a coherent beat between charge motion at ω and ω_{LO}.

function of 35 fs and centered at τ = 0. Fits to the selected cuts described above are shown in Fig. 2 (C to F), which in all cases are well described by a subpicosecond rise time to be discussed later. Subtraction of this slow response reveals the isolated coherent oscillations, $|\Delta r(\omega,\tau)|_{osc}$, that rapidly decay on a subpicosecond time scale commensurate with the slow rise. Figure 3A shows the pure oscillatory component of the normalized $|\Delta r(\omega,\tau)|^{norm}_{osc}$ for all THz probe energies. For $\omega < \omega_{LO}$, an ~5 times weaker, highly damped oscillation at a fixed frequency of ~0.5 THz is observed, which is the low-frequency limit of our measurements. The sign of the oscillations undergoes a π phase shift at $\omega = \omega_{LO}$, as expected when moving across the resonance. For $\omega > \omega_{LO}$, the oscillations gradually shift to higher frequencies with no further change in phase. The amplitude of the coherent oscillation is shown in Fig. 4A, showing a marked turn on at ω_{LO} and rising to a peak at 4.6 THz, corresponding to the spectral region where the lattice is least polarizable just above the reststrahlen band. The full width at half maximum (FWHM) of this peak is approximately 1 THz, comparable to the lifetime of the LO phonon at room temperature (*30*), broadened because of mode coupling with the highly damped and disordered motion of the organic cation.

The interaction of charge carriers with optical phonons is governed by a dressed Coulomb interaction, $W_q = \frac{V_q}{\varepsilon(\omega,\tau)}$, modified through dynamic screening by the correlated lattice dynamics described by the lattice dielectric function ε(ω,τ). The dielectric loss function, $-\mathrm{Im}[1/\tilde{\varepsilon}(\omega,\tau)]$, schematically plotted in Fig. 3B following (*31*), describes energy loss through interaction with optical phonons and is centered at ω_{LO}, with a very broad FWHM of ~1 THz due to mode coupling with the organic cation (*30*). The screening function, $\mathrm{Re}[1/\tilde{\varepsilon}(\omega,\tau)]$, renormalizes the charge in the dressed Coulomb interaction experienced by another charge under energy exchange of ħω and proceeds from an overscreened response at $\omega < \omega_{LO}$, where the lattice efficiently moves to oppose Coulomb forces between charge carriers, to $\omega > \omega_{LO}$, where the lattice cannot follow the electromagnetic perturbation and underscreens the interaction. The sign change in the coherent oscillation observed in Fig. 3A corresponds to the transition from an overscreened to an underscreened lattice response, where the lattice polarization moves from an in-phase to an out-of-phase response to the electromagnetic perturbation (*32*).

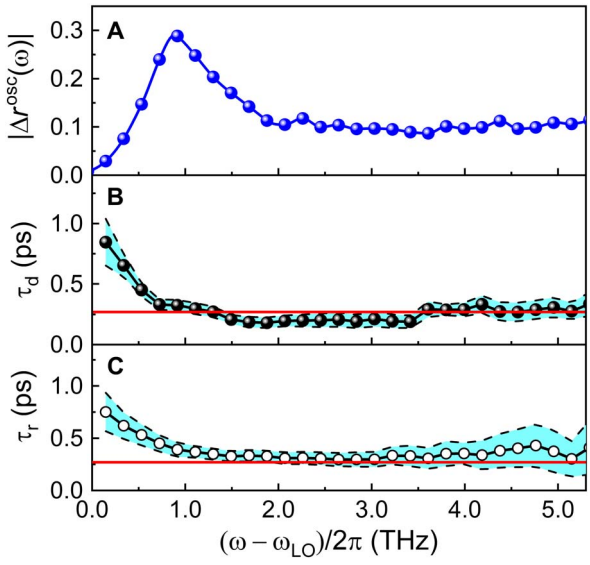

Fig. 4. Coherent beat amplitude, dephasing, and reflectivity rise times. (**A**) Amplitude of coherently oscillating component of the differential THz reflectivity. (**B**) The fitted dephasing time of the coherent oscillations and (**C**) the incoherent differential reflectivity rise time using the model discussed in the text. Shaded regions indicate 95% confidence regimes in the fitting. The red line in (B) and (C) marks one LO phonon period $2\pi/\omega_{LO}$ = 270 fs.

A Fourier transform of this normalized differential reflectivity along the pump-probe delay axis yields a 2D $|\Delta r(\omega, \omega_{osc})|_{osc}$ map shown in Fig. 3C. The map shows a coherent oscillation frequency $\omega_{osc} \propto \omega - \omega_{LO}$ or the beat frequency of the charge motion coupled to its lattice distortion. The coherent oscillations are governed by a single LO phonon at $\omega_{LO} = (2\pi)$ 3.7 THz, 15 meV, or 125 cm^{-1} as shown by the ω intercept at $\omega_{osc} = 0$ and the location of the phase flip in Fig. 3A. This is in agreement with time domain THz reflectivity measurements on single-crystal MAPI showing a single effective LO phonon at ~3.9 THz, which was temperature independent and strongly damped because of coupling with the dynamic orientational motion of the methylammonium (MA) cation (*30*). Recent ab initio calculations aimed at understanding the role that each phonon plays in polaron correlations in MAPI showed that multiple phonon branches contribute: bending (4 meV) and stretching (13 meV) modes of the Pb-I sublattice, as well as translational and librational modes of the organic cation (20 meV). At room temperature, the considerable broadening of the latter two lines merges to one single effective LO phonon, in excellent agreement with the observed $\hbar\omega_{LO}$ = 15 meV (*26*). The role of this stretching mode in the stabilization of large polarons was also highlighted in recent time-resolved optical Kerr measurements on $CH_3NH_3PbBr_3$ and density functional theory calculations in (*12*).

The Fröhlich electron-phonon coupling constant α can subsequently be calculated by (*15*)

$$\alpha = \frac{e^2}{\hbar\omega_{LO}} \frac{1}{4\pi\varepsilon_0} \left(\frac{m^*}{2\hbar\omega_{LO}}\right)^{\frac{1}{2}} \left(\frac{1}{\varepsilon_\infty} - \frac{1}{\varepsilon_s}\right) \quad (1)$$

where m^* is the effective mass and ε_s and ε_∞ are the dielectric constants below and above the related reststrahlen band, respectively, with parameters given in the Supplementary Materials. This yields a value of α = 2.0 (*15*). The polaron binding energy can then be calculated by $E_P = -\hbar\omega_{LO}[\alpha + 0.0158\alpha^2 + 0.00081\alpha^3] \approx 30$ meV, and the radius of the polaron can be estimated by $r_p = \sqrt{\frac{\hbar}{2m^*\omega_{LO}}} \approx$ 3.5 nm or approximately six unit cells. These values agree with previous works (*12*, *33*) and place MAPI in the intermediate coupling regime, similar to other metal halides.

The dynamics of $|\Delta r(\tau)|/|r_0|$ is described by fitting the data to a slow exponential rise $R_1(\tau) = \theta(\tau)(a - be^{-\tau/\tau_r})$ and a damped oscillator $R_2(\tau) = \theta(\tau)c\, e^{-\tau/\tau_d}\cos[(\omega-\omega_{LO})\tau + \varphi]$. The $R_1(\tau)$ component models the dynamics of polaron formation with a time constant τ_r, and $R_2(\tau)$ describes the quantum beat dephasing with a time constant τ_d. The results of these fits are shown in Fig. 4 (B and C), with both time constants comparable and increasing near the resonance condition $\omega = \omega_{LO}$ and relatively constant at 200 to 300 fs above 5 THz. This corresponds to approximately one LO phonon period (270 fs), indicating rapid dephasing potentially through mode coupling with the organic cation (*30*) or through lattice anharmonicity (*17*). We propose that the observed increase in both τ_d and τ_r as $\omega \rightarrow \omega_{LO}$ may be a signature of this dissipative coupling to other modes, as they are expected to contribute less when the scattering process is perfectly resonant with the single LO phonon mode. The similarity of the incoherent rise time and the coherent dephasing time suggests a similar microscopic mechanism, justifying the assignment of the incoherent rise time to the formation of a quasi-stable polaron. In addition, as was pointed out in (*34*, *35*), the formation of a stable polaron after injection of a bare charge is only completed after coherent phonons emitted through the initial relaxation process no longer interact with the charge wave packet. At higher THz probe energies, polaron excitations can produce unbound phonons with nonzero momentum *q* and scattered polarons with momentum *k*-*q*. These unbound phonons rapidly decouple from the polaron, leading to a faster formation time. Further quantum kinetic calculations will be required to elucidate the origin of this observed increase in the formation time near resonance. Our results show that polaron correlations are present almost instantaneously after charge injection, in agreement with femtosecond optical Kerr measurements (*12*), and that their coherent interaction with their radiated LO phonons decays on a time scale comparable to the phonon period. These results are supported by recent ab initio molecular dynamics calculations showing subpicosecond formation of electron and hole polarons caused by coupling to thermal vibrations of the inorganic cage (*16*).

In summary, we report the measurement of intraband quantum beats arising from polaron correlations in MAPI, as they are formed on a subpicosecond time scale at room temperature. The origin of the quantum beat can be understood by considering the relative motion of the charge carriers to their coupled LO phonon cloud. We find that a single effective LO phonon at $\omega_{LO} = (2\pi)$ 3.7 THz is coupled to electronic motion, which has been identified as a mixture of two modes, a Pb-I stretch and a translational and librational motion of the MA cation. The slow rise time connected to polaron formation and the dephasing time of the coherent oscillation are highly damped at approximately one phonon period. These measurements of correlated electron-phonon motion in the band provide direct and quantitative evidence that stable polarons exist in MAPI at room temperature. Direct experimental signatures of polarons in hybrid organic-inorganic perovskites have proven difficult until now, and first-principles calculations are impeded by the large number of atoms involved. We anticipate that confirmation of the polaronic nature of carriers in the lead halide perovskites will have direct consequences for the morphological and compositional engineering of perovskite devices, as it is clear that optimizing

electronic properties cannot be accomplished without accounting for the intricate, correlated dance of the charge with the lattice.

MATERIALS AND METHODS

MAPI crystal synthesis

Single crystals of MAPI were grown from γ-butyrolactone (GBL) by the temperature-rising method with procedures similar to previous works (*36*). The binary precursors, PbI_2 (5 N; Sigma-Aldrich) and methylammonium iodide (Sigma-Aldrich), were mixed with a stochiometric ratio of 1:1 in GBL solvent at 60° to 70°C to form a 1.4 M solution. To facilitate the growth of single crystals, the as-prepared solution was then gradually heated to 100°–110°C. Once single crystals had nucleated, the solution temperature was kept constant to promote the continuous growth of large crystals. The as-grown single crystals were harvested after a period of several hours, yielding a cubic centimeter–sized single crystal with large and flat facets suitable for THz spectroscopy.

Time-resolved multi-THz spectroscopy

TRTS measurements were performed using an all-air plasma-based system providing single-cycle, coherently detected THz pulses continuously spanning the range of 1 to 20 THz as shown in figs. S12 and S13. Broadband THz light was generated by a two-color laser plasma by focusing 800-nm, 35-fs pulses with an energy of 1 mJ and their second harmonic into dry air (*23*). The reflected THz transients were detected with an air-biased coherent detection scheme using the generated second harmonic of the 800-nm sampling beam in a biased plasma as a phase-sensitive probe of the instantaneous THz field (*27*). No compensation for the group delay dispersion between 800- and 400-nm pulses was performed, so the peak THz field strength was limited to ~20 kV/cm. A near-infrared pump pulse excites charge carriers at the band edge at a center wavelength of ~795 nm (1.56 eV), a fluence of 200 μJ/cm^2, and a pump-probe delay τ. Optical pump–THz probe experiments were performed at normal incidence reflection from the $\langle 11\bar{1}\rangle$ facet of a large MAPI crystal (size, ~1 cm^3) of rhombic dodecahedral habit. Other facets showed similar results and are shown in the Supplementary Materials. Time- and energy-resolved transient THz reflectivity maps were obtained by Fourier analysis of the reflected THz pulses without photoexcitation, $\tilde{E}_{\mathrm{ref}}(\omega)$, and with photoexcitation, $\tilde{E}_{\mathrm{pump}}(\omega,\tau)$, at a delay time τ. Differential reflectivity was defined as $\frac{\Delta\tilde{r}(\omega,\tau)}{\tilde{r}_0(\omega)} = (\tilde{E}_{\mathrm{pump}} - \tilde{E}_{\mathrm{ref}})/\tilde{E}_{\mathrm{ref}}$ and was complex-valued with full amplitude, as shown in the main text, and phase information is given in the Supplementary Materials. Measurements were performed at 295 K in the tetragonal phase of MAPI under dry-purged gas conditions with no evidence of surface degradation during the map acquisition time of ~20 hours.

SUPPLEMENTARY MATERIALS

Supplementary material for this article is available at http://advances.sciencemag.org/cgi/content/full/5/5/eaaw5558/DC1

Fig. S1. Static dielectric function of MAPI.
Fig. S2. Conductivity of MAPI at τ =1 ps.
Fig. S3. Phase of pump-induced differential THz reflectivity at the $\langle 11\bar{1}\rangle$ facet.
Fig. S4. Amplitude of pump-induced differential THz reflectivity at the ⟨100⟩ facet.
Fig. S5. Time domain coherent oscillations of THz reflectivity without slow rise component at ⟨100⟩ facet.
Fig. S6. Fourier domain coherent oscillations of THz reflectivity without slow rise component at ⟨100⟩ facet.
Fig. S7. Time constants at ⟨100⟩ facet.
Fig. S8. Amplitude of pump-induced differential THz reflectivity at ⟨111⟩ facet.
Fig. S9. Time domain coherent oscillations of THz reflectivity without slow rise component at ⟨111⟩ facet.
Fig. S10. Fourier domain coherent oscillations of THz reflectivity without slow rise component at ⟨111⟩ facet.
Fig. S11. Time constants at ⟨111⟩ facet.
Fig. S12. Electric field in time domain of the reference THz probe pulse.
Fig. S13. Power spectrum of the reference THz probe pulse.
Fig. S14. Pump-induced THz reflectivity change for different probe field strengths.
Table S1. Parameters describing MAPI dielectric properties.
Reference (*37*)

REFERENCES AND NOTES

1. M. Bonn, K. Miyata, E. Hendry, X.-Y. Zhu, Role of dielectric drag in polaron mobility in lead halide perovskites. *ACS Energy Lett.* **2**, 2555–2562 (2017).
2. M. A. Green, A. Ho-Baillie, Perovskite solar cells: The birth of a new era in photovoltaics. *ACS Energy Lett.* **2**, 822–830 (2017).
3. C. C. Stoumpos, M. G. Kanatzidis, The Renaissance of halide perovskites and their evolution as emerging semiconductors. *Acc. Chem. Res.* **48**, 2791–2802 (2015).
4. S. D. Stranks, H. J. Snaith, Metal-halide perovskites for photovoltaic and light-emitting devices. *Nat. Nanotechnol.* **10**, 391–402 (2015).
5. K. Miyata, T. L. Atallah, X.-Y. Zhu, Lead halide perovskites: Crystal-liquid duality, phonon glass electron crystals, and large polaron formation. *Sci. Adv.* **3**, 1701469 (2017).
6. K. X. Steirer, P. Schulz, G. Teeter, V. Stevanovic, M. Yang, K. Zhu, J. J. Berry, Defect tolerance in methylammonium lead triiodide perovskite. *ACS Energy Lett.* **1**, 360–366 (2016).
7. T. D. Lee, F. E. Low, D. Pines, The motion of slow electrons in a polar crystal. *Phys. Rev.* **90**, 297–302 (1953).
8. A. Leitenstorfer, S. Hunsche, J. Shah, M. C. Nuss, W. H. Knox, Femtosecond charge transport in polar semiconductors. *Phys. Rev. Lett.* **82**, 5140–5143 (1999).
9. M. Betz, G. Göger, A. Laubereau, P. Gartner, L. Bányai, H. Haug, K. Ortner, C. R. Becker, A. Leitenstorfer, Subthreshold carrier-LO phonon dynamics in semiconductors with intermediate polaron coupling: A purely quantum kinetic relaxation channel. *Phys. Rev. Lett.* **86**, 4684–4687 (2001).
10. H. Frölich, Electrons in lattice fields. *Adv. Phys.* **3**, 325–361 (1954).
11. X.-Y. Zhu, V. Podzorov, Charge carriers in hybrid organic–inorganic lead halide perovskites might be protected as large polarons. *J. Phys. Chem. Lett.* **6**, 4758–4761 (2015).
12. K. Miyata, D. Meggiolaro, M. T. Trinh, P. P. Joshi, E. Mosconi, S. C. Jones, F. D. Angelis, X.-Y. Zhu, Large polarons in lead halide perovskites. *Sci. Adv.* **3**, e1701217 (2017).
13. R. P. Feynman, Slow electrons in a polar crystal. *Phys. Rev.* **97**, 660–665 (1955).
14. H. M. Zhu, K. Miyata, Y. Fu, J. Wang, P. P. Joshi, D. Niesner, K. W. Williams, S. Jin, X.-Y. Zhu, Screening in crystalline liquids protects energetic carriers in hybrid perovskites. *Science* **353**, 1409–1413 (2016).
15. J. T. Devreese, Polarons. *AIP Conf. Proc.* **678**, 3–56 (2003).
16. F. Ambrosio, J. Wiktor, F. De Angelis, A. Pasquarello, Origin of low electron–hole recombination rate in metal halide perovskites. *Energy Environ. Sci.* **11**, 101–105 (2018).
17. O. Yaffe, Y. Guo, L. Z. Tan, D. A. Egger, T. Hull, C. C. Stoumpos, F. Zheng, T. F. Heinz, L. Kronik, M. G. Kanatzidis, J. S. Owen, A. M. Rappe, M. A. Pimenta, L. E. Brus, Local polar fluctuations in lead halide perovskite crystals. *Phys. Rev. Lett.* **118**, 136001 (2017).
18. D. M. Monahan, L. Guo, J. Lin, L. Dou, P. Yang, G. R. Fleming, Room-temperature coherent optical phonon in 2D electronic spectra of $CH_3NH_3PbI_3$ perovskite as a possible cooling bottleneck. *J. Phys. Chem. Lett.* **8**, 3211–3215 (2017).
19. T. Ghosh, S. Aharon, L. Etgar, S. Ruhman, Free carrier emergence and onset of electron-phonon coupling in methylammonium lead halide perovskite films. *J. Am. Chem. Soc.* **139**, 18262–18270 (2017).
20. G. Batignani, G. Fumero, A. R. S. Kandada, G. Cerullo, M. Gandini, C. Ferrante, A. Petrozza, T. Scopigno, Probing femtosecond lattice displacement upon photo-carrier generation in lead halide perovskite. *Nat. Commun.* **9**, 1971 (2018).
21. F. Thouin, D. A. Valverde-Chávez, C. Quarti, D. Cortecchia, I. Bargigia, D. Beljonne, A. Petrozza, C. Silva, A. R. S. Kandada, Phonon coherences reveal the polaronic character of excitons in two-dimensional lead-halide perovskites (2018); arXiv: 1807.10539 [cond-mat.mtrl-sci].
22. C. S. Ponseca Jr., T. J. Savenije, M. Abdellah, K. Zheng, A. Yartsev, T. Pascher, T. Harlang, P. Chabera, T. Pullerits, A. Stepanov, J.-P. Wolf, V. Sundström, Organometal halide perovskite solar cell materials rationalized: Ultrafast charge generation, high and microsecond-long balanced mobilities, and slow recombination. *J. Am. Chem. Soc.* **136**, 5189–5192 (2014).

23. D. A. Valverde-Chávez, C. S. Ponseca Jr., C. C. Stoumpos, A. Yartsev, M. G. Kanatzidis, V. Sundström, D. G. Cooke, Intrinsic femtosecond charge generation dynamics in single crystal $CH_3NH_3PbI_3$. *Energy Environ. Sci.* **8**, 3700–3707 (2015).
24. S. A. Bretschneider, I. Ivanov, H. I. Wang, K. Miyata, X. Zhu, M. Bonn, Quantifying polaron formation and charge carrier cooling in lead-iodide perovskites. *Adv. Mater.* **30**, 1707312 (2018).
25. B. Guzelturk, R. A. Belisle, M. D. Smith, K. Bruening, R. Prasanna, Y. Yuan, V. Gopalan, C. J. tASSONE, H. I. Karunadasa, M. D. McGehee, A. M. Lindenberg, Terahertz emission from hybrid perovskites driven by ultrafast charge separation and strong electron-phonon coupling. *Adv. Mater.* **30**, 1704737 (2018).
26. M. Schlipf, S. Poncé, F. Giustino, Carrier lifetimes and polaronic mass enhancement in the hybrid halide perovskite $CH_3NH_3PbI_3$ from multiphonon Fröhlich coupling. *Phys. Rev. Lett.* **121**, 086402 (2018).
27. J. Dai, X. Xie, X.-C. Zhang, Detection of broadband terahertz waves with a laser-induced plasma in gases. *Phys. Rev. Lett.* **97**, 103903 (2006).
28. P. Gaal, W. Kuehn, K. Reimann, M. Woerner, T. Elsaesser, R. Hey, Internal motions of a quasiparticle governing its ultrafast nonlinear response. *Nature* **450**, 1210–1213 (2007).
29. C. La-o-vorakiat, H. Xia, J. Kadro, T. Salim, D. Zhao, T. Ahmed, Y. M. Lam, J.-X. Zhu, R. A. Marcus, M.-E. Michel-Beyerle, E. E. M. Chia, Phonon mode transformation across the orthohombic-tetragonal phase transition in a lead iodide perovskite $CH_3NH_3PbI_3$: A terahertz time-domain spectroscopy approach. *J. Phys. Chem. Lett.* **7**, 1–6 (2016).
30. M. Nagai, T. Tomioka, M. Ashida, M. Hoyano, R. Akashi, Y. Yamada, T. Aharen, Y. Kanemitsu, Longitudinal optical phonons modified by organic molecular cation motions in organic-inorganic hybrid perovskites. *Phys. Rev. Lett.* **121**, 145506 (2018).
31. L. M. Herz, How lattice dynamics moderate the electronic properties of metal-halide perovskites. *J. Phys. Chem. Lett.* **9**, 6853–6863 (2018).
32. R. Huber, F. Tauser, A. Brodschelm, M. Bichler, G. Abstreiter, A. Leitenstorfer, How many-particle interactions develop after ultrafast excitation of an electron-hole plasma. *Nature* **414**, 286–289 (2001).
33. M. Sendner, P. K. Nayak, D. A. Egger, S. Beck, C. Müller, B. Epding, W. Kowalsky, L. Kronik, H. J. Snaith, A. Pucci, R. Lovrin čić, Optical phonons in methylammonium lead halide perovskites and implications for charge transport. *Materials Horiz.* **3**, 613–620 (2016).
34. C. Kübler, H. Ehrke, R. Huber, R. Lopez, A. Halabica, R. F. Haglund Jr., A. Leitenstorfer, Coherent structural dynamics and electronic correlations during an ultrafast insulator-to-metal phase transition in VO2. *Phys. Rev. Lett.* **99**, 116401 (2007).
35. L.-C. Ku, S. Trugman, Quantum dynamics of polaron formation. *Phys. Rev. B* **75**, 014307 (2007).
36. Y. He, W. Ke, G. C. B. Alexander, K. M. McCall, D. G. Chica, Z. Liu, I. Hadar, C. C. Stoumpos, B. W. Wessels, M. G. Kanatzidis, Resolving the energy of γ-ray photons with $MAPbI_3$ single crystals. *ACS Photonics* **5**, 4132–4138 (2018).
37. G. Giorgi, J.-I. Fujisawa, H. Segawa, K. Yamashita, Small photocarrier effective masses featuring ambipolar transport in methylammonium lead iodide perovskite: A density functional analysis. *J. Phys. Chem. Lett.* **4**, 4213–4216 (2013).

Acknowledgments

Funding: D.G.C. and M.S. acknowledge financial support from NSERC, CFI, and FQRNT. The work at Northwestern University (synthesis and fundamental studies of halide perovskites) was supported by the U.S. DOE, Office of Science (grant SC0012541). **Author contributions:** Conceptualization: D.G.C.; data curation: Y.L.; formal analysis: Y.L., B.J.D., and D.G.C.; funding acquisition: M.S., M.G.K., and D.G.C.; investigation: Y.L., B.J.D., C.S.P., and D.A.V.-C.; methodology: Y.L. and D.G.C.; project administration: D.G.C.; resources: Y.H. and M.G.K.; software: Y. L., B.J.D., D.A.V.-C., and D.G.C.; supervision: M.S., M.G.K., and D.G.C.; validation: D.G.C.; visualization: Y.L. and B.J.D.; writing (original draft): Y.L.; writing (review and editing): B.J.D., C.S.P., M.S., M.G.K., and D.G.C. **Competing interests:** The authors declare that they have no competing interests. **Data and materials availability:** All data needed to evaluate the conclusions in the paper are present in the paper and/or the Supplementary Materials. Additional data related to this paper may be requested from the authors.

Submitted 4 January 2019
Accepted 17 April 2019
Published 31 May 2019
10.1126/sciadv.aaw5558

Citation: Y. Lan, B. J. Dringoli, D. A. Valverde-Chávez, C. S. Ponseca, M. Sutton, Y. He, M. G. Kanatzidis, D. G. Cooke, Ultrafast correlated charge and lattice motion in a hybrid metal halide perovskite. *Sci. Adv.* **5**, eaaw5558 (2019).